Bull Volcanol (1997) 58:515–527

ORIGINAL PAPER

J. K. Russell · M. V. Stasiuk

Characterization of volcanic deposits with ground-penetrating radar

Received: 10 May 1996 / Accepted: 27 December 1996

Abstract Field-based studies of surficial volcanic deposits are commonly complicated by a combination of poor exposure and rapid lateral variations controlled by unknown paleotopography. The potential of ground-penetrating radar (GPR) as an aid to volcanological studies is shown using data collected from traverses over four well-exposed, Recent volcanic deposits in western Canada. The deposits comprise a pumice airfall deposit (3–4 m thick), a basalt lava flow (3–6 m thick), a pyroclastic flow deposit (15 m thick), and an internally stratified pumice talus deposit (60 m thick). Results show that GPR is effective in delineating major stratigraphic contacts and hence can be used to map unexposed deposits. Different volcanic deposits also exhibit different radar stratigraphic character, suggesting that deposit type may be determined from radar images. In addition, large blocks within the pyroclastic deposits are detected as distinctive point diffractor patterns in the profiles, showing that the technique has potential for providing important grain-size information in coarse poorly sorted deposits. Laboratory measurements of dielectric constant (K') are reported for samples of the main rock types and are compared with values of K' for the bulk deposit as inferred from the field data. The laboratory values differ significantly from the "field" values of K'; these results suggest that the effectiveness of GPR at any site can be substantially improved by initial calibration of well-exposed locations.

Editorial responsibility: M. Rosi

J. K. Russell (✉)
Department of Earth and Ocean Sciences, Geological Sciences Division, University of British Columbia, Vancouver, B.C., Canada
e-mail: russell@perseus.geology.ubc.ca

M. V. Stasiuk
Environmental Science Division, Lancaster University, Lancaster, UK
e-mail: mark.s@lancaster.ac.uk

Key words Ground-penetrating radar · Volcanic deposits · Stratigraphy · Dielectric constant · Radar velocity · Pyroclastic flow · Airfall · Lava

Introduction

Studies of surficial volcanic deposits are commonly limited by incomplete exposure. Estimates of the physical properties, distributions, thicknesses, and internal structures of the deposits are usually derived from studies on a few well-dissected outcrops. Ground-penetrating radar (GPR) is a portable geophysical technique which can provide ancillary information on the unexposed parts of deposits, thereby facilitating many volcanological studies. In this paper we demonstrate the potential of this technique, relatively underutilized in geological field work, to map volcanic deposits.

We surveyed a variety of Recent volcanic deposits, primarily to investigate the utility of GPR in the characterization of such volcanic deposits. Specifically, GPR data were collected along four traverses overlying volcanic deposits in western Canada, north of Vancouver, British Columbia. Locations of the traverses are shown in Fig. 1 and described in Table 1. The sites include a basalt lava flow (Fig. 2a), a thinly vegetated airfall pumice deposit (Fig. 2b), a pyroclastic block and ash flow deposit underlying fluvial deposits (Fig. 2c, d), and a thick, near-vent accumulation of slumped tephra (Fig. 2e, f). These four sites span a wide range of volcanic deposit types and provide a good test of the capabilities of GPR. The sites were also chosen, in part, because they have excellent cross-sectional exposure, thereby affording the opportunity for direct comparison between the actual deposits and the ground-penetrating radar data. The results show that GPR can effectively define deposit contacts and can elucidate finer-scale internal features.

As a complement to the field study, we present laboratory measurements of dielectric properties of rock

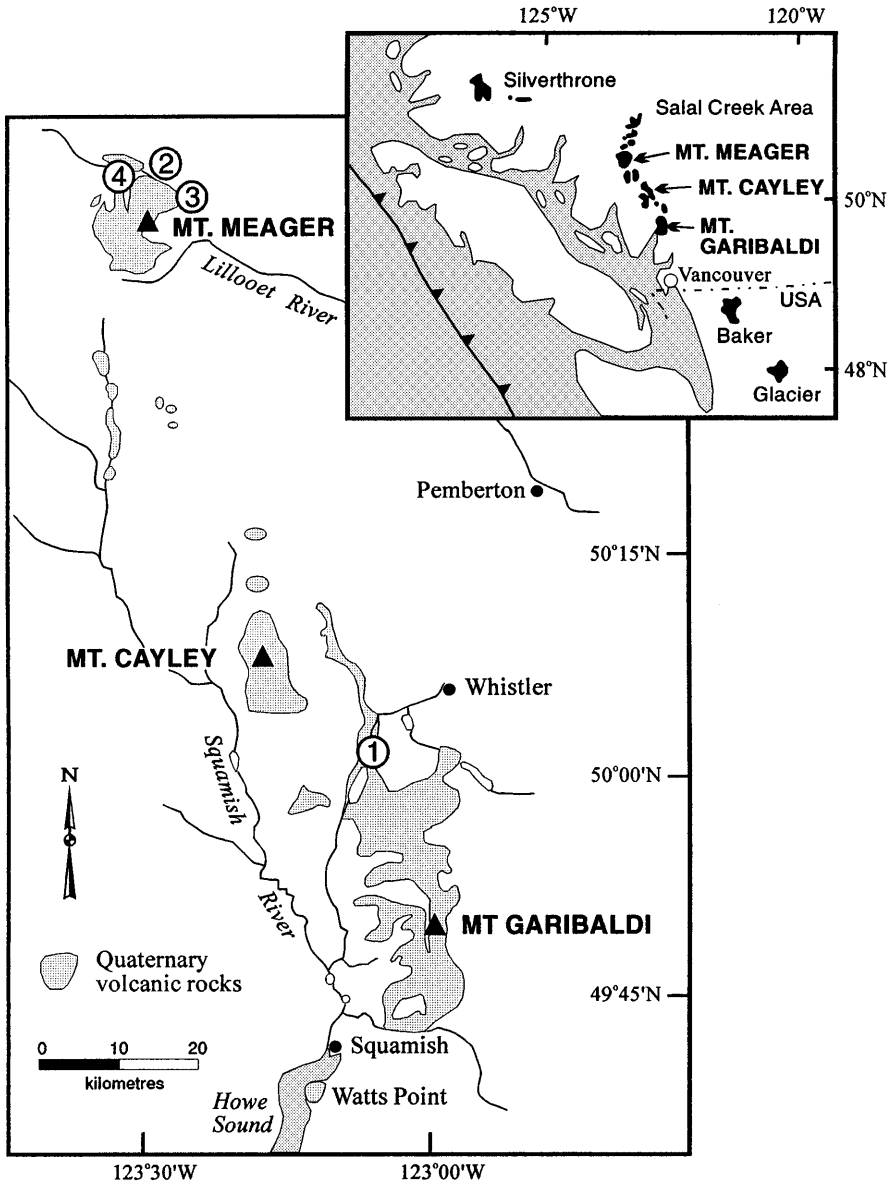

Fig. 1 Locations of ground-penetrating radar (GPR) surveys shown against the distribution of Quaternary volcanoes in southwest British Columbia (see *inset*). Survey sites include: *1* basalt lavas within the Garibaldi belt, and *2–4* pyroclastic deposits associated with the 2360 BP eruption of Mt. Meager

Table 1

Site	Deposit	Survey profile (length; orientation)	Station spacing (m)/ total stations	Time window(ns)/Stacks	Gain type
1	Basalt lava flow	40 m; N to S	0.5/81	512/128	AGC
2	Pumice fall deposit	51 m; W to E	1/52	512/128	AGC
3	Pyroclastic flow	191 m; W to E	1/192	512/ 64	AGC
4a	Pumice talus cone	181 m; W to E	2/93	2048/512	AGC
4b	Pumice talus cone	50 m; W to E	1/51	512/256	Constant

NOTE: Surveys used a 400-V transmitter and a 0.6-m separation between transmitter and receiver antennae

samples collected from several of the traverse sites. Dielectric properties are the dominant physical property affecting the velocity, attenuation, and reflection of electromagnetic (EM) waves in the subsurface. These results allow a preliminary investigation of the relationship between laboratory measurements of K' based on small samples and the observed bulk or effective dielectric constant of the deposits as a whole.

Fig. 2 Photographs of field exposures of volcanic deposits underlying GPR surveys and showing: **a** basalt lava flow exposed in road cut; **b** pumice fall deposit exposed on logging road; **c** overall character of pyroclastic flow deposit exposed on banks of Lillooet River; **d** pumice blocks and charred logs within the pyroclastic flow deposit; **e** large-scale structure of reworked pumice talus cone on southern banks of Lillooet River; and **f** fine-scale layering and structure of pumice talus deposit overlying massive rock avalanche deposit ▶

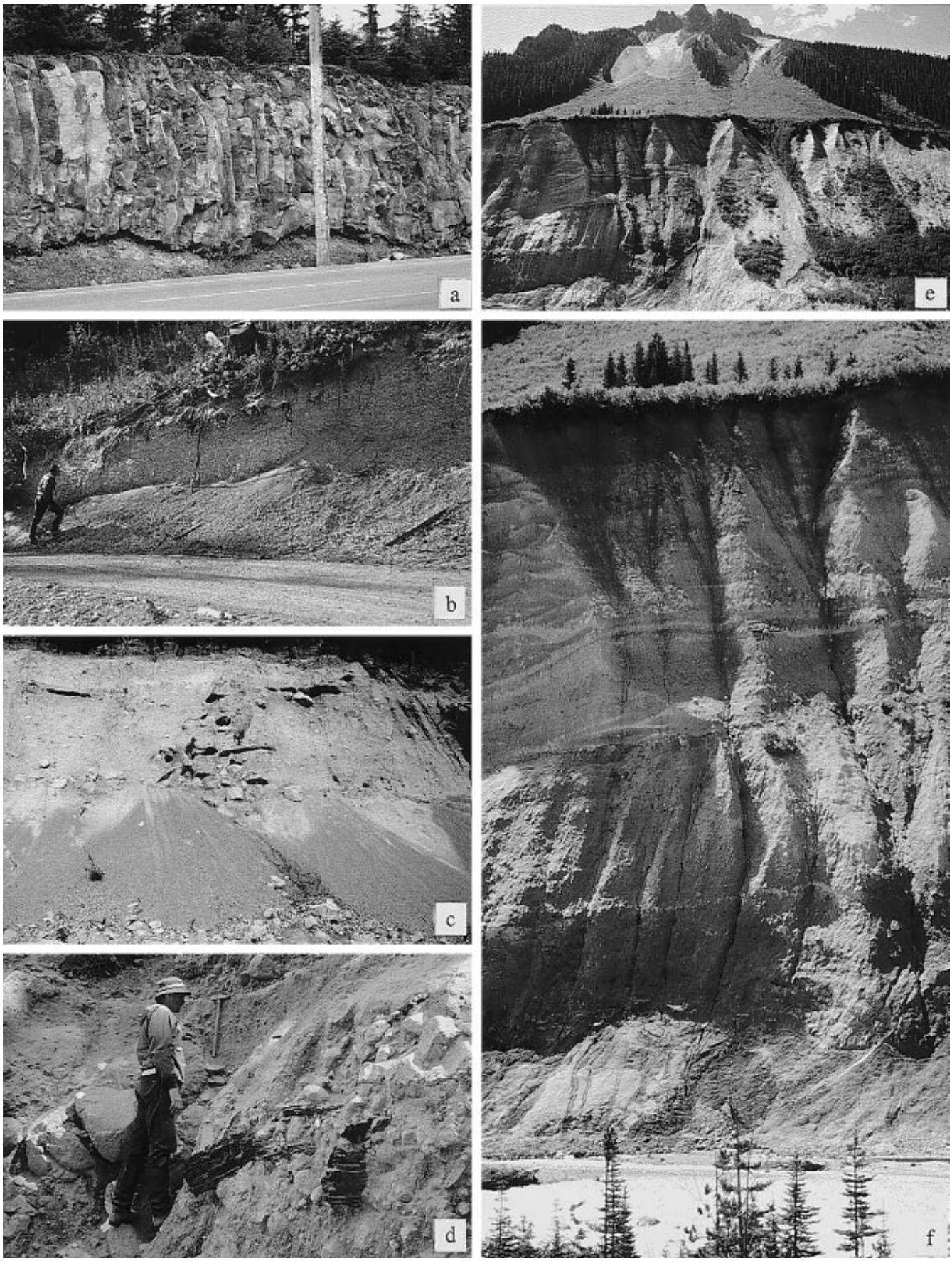
a
e
b
c
d
f

Ground-penetrating radar

Ground-penetrating radar uses EM waves in the Megahertz (MHz) frequency range to image subsurface variations in electrical properties; conceptually it is the EM analog of reflection seismology (e.g., Ardon 1985). Fundamental principles of the technique are described in Davis and Annan (1989).

Ground-penetrating radar has three main attributes as a geophysical mapping tool. Firstly, GPR can acquire subsurface data over large areas at low cost because it collects rapidly, the instrument is relatively inexpensive, and it requires no more than two people to operate. Secondly, it is portable and robust enough to be operated in remote and difficult field locations. Finally, the data are displayed while collected and, commonly with minimal processing, can provide interpretable results bearing on deposit thickness, character, and internal structure (e.g., Davis and Annan 1989; Smith and Jol 1992). This means that collection conditions or traverse plans can be evaluated in the field and changed, if necessary, to improve the results of the GPR survey.

In recent years, the use of GPR for imaging the shallow subsurface has steadily increased. It has been widely used in the study of glaciers for the determination of thicknesses and internal structure of ice sheets (e.g., Jezek and Thompson 1982; Clarke and Cross 1989), in the fields of civil and geotechnical engineering (e.g., Fowler 1981; Ardon 1985; Holloway et al. 1986), and in archeology (e.g., Vaughan 1986; Goodman 1994; Camerlynck et al. 1994). It is also a well-established method in the field of environmental geophysics and is frequently used for imaging near-surface unlithified deposits (e.g., Annan and Davis 1977; Davis and Annan 1989; Jol and Smith 1991) and aquifers (e.g., Knoll et al. 1991; Rea et al. 1994).

Ground-penetrating radar techniques are also applicable to studies of bedrock and a wide variety of lithified geological deposits. For example, surveys have been used to image shallow structures in coarse-grained, well-sorted sedimentary deposits (e.g., Jol and Smith 1992; Smith and Jol 1992). Other diverse geological applications include studies of: the subsurface structure of a meteor impact crater (Pilon et al. 1991), fracture distributions in granites (Holloway et al. 1986), reef stratigraphy in a Paleozoic limestone (Pratt and Miall 1993), structures in folded rocks (Liner and Liner 1995), and the morphology of a subglacial volcano (Gilbert et al. 1996). Furthermore, the development of higher power transmitters (e.g., 1000 V), lower frequency antennae (e.g. <50 MHz), and more focused beams has improved the technique's effectiveness for geological studies.

Volcanic deposits are appropriate for the use of GPR because they are typically thin (<100 m), surficial, compositionally homogeneous deposits, and can be electrically resistive. These features facilitate deep penetration of radar energy (e.g., Annan and Davis 1977; Davis and Annan 1989). In addition, the broad grain-size distribution which typifies poorly sorted pyroclastic deposits overlaps the resolution limits of higher frequency GPR (e.g., Davis and Annan 1989), and hence represents detectable information. However, with few exceptions (e.g., Clarke and Cross 1989; McCoy et al. 1992; Stasiuk and Russell 1993; Gilbert et al. 1996), GPR techniques have not been used to study problems associated with volcanoes and or volcanic deposits.

Field surveys

Details concerning the four GPR traverse sites are summarized in Table 1 and discussed below. Excluding the basalt lava flow (site 1), all volcanic deposits originate from the 2360 BP eruption of Mount Meager (Nasmith et al. 1967; Read 1977; Clague et al. 1995). Further details concerning the nature and distribution of the deposits derived from the 2360 BP eruption are described in detail by Stasiuk and Russell (1990). Background information on the Cheakamus basalt lava flow can be found in Green et al. (1988) and Nicholls et al. (1982).

Acquisition of radar data

A commercial GPR system (PulseEKKO IV, SSI) with a 100-MHz antennae and 400-V transmitter was used for each survey. The surveys were run in profiling mode with a fixed offset of 0.6 m between transmitter and receiver antennae. Data were vertically stacked 64–512 times to improve the signal-to-noise ratio. Other acquisition parameters for each profile are summarized in Table 1.

The surveys were run within a few meters of the top of the geological exposures, thereby ensuring that the radar data could be correlated directly with features visible in the deposits. There was no evidence of primary reflectors from the face of the exposures. Although some of the surveys were run over rough terrain (e.g., talus and fallen trees), an attempt was made to maintain constant elevation throughout the survey, thereby eliminating any need for post-collection elevation corrections.

Data were collected with a fixed gain but, for interpretation and presentation purposes, were analyzed with no gain, as well as scaled with constant gain or automatic gain control (AGC is a standard option within the pEIV software). Gain artificially increases the amplitudes of signals recorded in the traces and is used to visually compensate for decreased amplitudes reflected from greater depths. Increasing the gain can enhance deeper reflecting surfaces but saturates the shallow signal. Furthermore, it is only effective where reflected amplitudes are significantly larger than background noise amplitudes (large signal-to-noise ratio).

Two-way travel times are converted to depth wherever the velocity of the radar in the deposit is known. The radar velocities and the dielectric properties of these deposits were not known a priori and an alternative strategy was therefore used for sites 1–3; a velocity was chosen that gave the best "depth" match between well-defined stratigraphic features in the deposit and corresponding reflections in the GPR profile.

Results

Cheakamus Valley basalt lava (site 1)

A 40-m GPR survey was carried out on the horizontal, upper surface of a basaltic lava flow exposed in cross section along a roadcut (Highway 99) approximately 15 km south of Whistler, British Columbia, and immediately north of Brandywine Falls provincial park (Fig. 1; Table 1). The basalt is holocrystalline and lithologically homogeneous (Nicholls et al. 1982; Green et al. 1988). The lava flow is 3–6 m thick, poorly vesicular and has both regular vertical columnar joints (0.7 m spacing) and irregular subhorizontal joints (Fig. 2a). The lava flow shows a crude stratification that results from discontinuous zones of concentrations of subhorizontal jointing; an example of this planar structure is visible in Fig. 2a approximately 1 m from the flow base. The flow lies directly on a poorly indurated, irregular, scoriaceous autobreccia up to 1 m thick. Lava flow and breccia overlie laterally extensive clay-rich glacial tills which are several meters thick at this location.

The results of the GPR survey are shown in Fig. 3 as three profiles comprising identical data. Figures 3a and b have vertical exaggeration and are displayed with different values of AGC gain. The uppermost profile is plotted with minimal gain and shows three main features. Firstly, each trace clearly shows the air and surface waves. Secondly, there seems to be two right-dipping contacts whose upper parts are located at times of 70–90 ns and horizontal distances along the traverse of 0 and 7 m. These are, in fact, well-defined limbs of two hyperbolic point diffractor patterns; other fainter point diffractors can be seen at depth (110–140 ns) towards the right end of the traverse. Such hyperbolic point diffractors are manifested in GPR sections as characteristic hyperbolae-shaped surfaces, and are caused by the reflection of energy from sharp edges or embedded discontinuities close in size to the resolution of the method (e.g., Hatton et al. 1986). Thirdly, at this value of AGC gain there is a depth (time) below which there is no apparent signal; this depth appears to increase to the right.

The same data at higher gain (Fig. 3b) show more clearly a collection of overlapping point diffractors in a thin, right-dipping zone. The limbs of the hyperbolae cross over each other, which produces a region in the GPR section where the data have a cross-hatched to hummocky appearance. A particularly clear example of

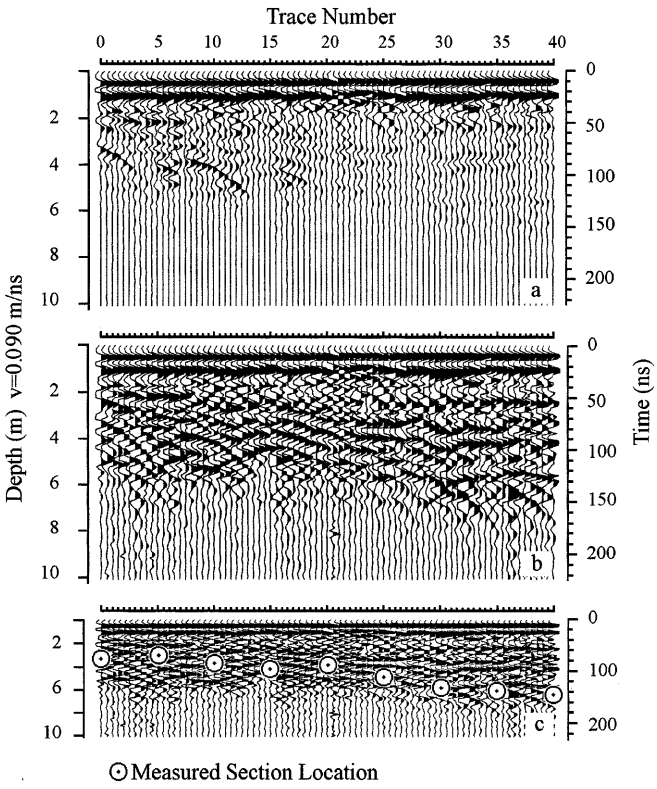

Fig. 3a–c Radar profiles from traverse over basalt lava flow (site 1). Radar results are shown with 2× vertical exaggeration and automatic gain control (AGC) gains of **a** 0.002, **b** 0.015, and **c** with no vertical exaggeration and AGC gain of 0.015. *Open circles* in **c** denote field-measured thicknesses of basalt lava and mark the contact between massive lava and basal flow breccia and/or underlying glacial till

crossed hyperbola limbs can be seen at a time of approximately 140 ns and a traverse distance of 31 m. Above the region characterized by the cross-hatched or hummocky appearance are irregular and discontinuous reflectors. Below this region there is a "dead zone" of weak received energy.

We interpret the diffraction events as either the result of sharp irregularities in the lava flow base or as reflections from blocks in the basal autobreccia. The severe decrease in amplitudes below 150 ns is interpreted to be caused by attenuation of transmitted energy by the underlying till. Glacial tills with high clay contents are electrically conductive and hence absorb EM energy, thereby limiting the depth of radar penetration.

Figure 3c shows the same data as in Fig. 3b, but with no vertical exaggeration. Superimposed on these data are nine points representing the measured thicknesses of the lava flow (circles). The average velocity used to convert two-way travel time to depth for these profiles was determined by correlating the top of the cross-hatched or hummocky zone in the profile with the corresponding field measurement of flow thickness at position 30 m. The correspondence between the other circles and the top of this zone (Fig. 3c) suggests that the velocity does not change significantly over the length of

the profile and corroborates the overall interpretation of the GPR profile. Figure 3 also shows a strong, nearly continuous stratification that crudely parallels the base of the flow and lies just above the zone characterized by the intense cross-hatched or hummocky pattern (Fig. 3c). We interpret these to be reflections from subhorizontal joint surfaces (Fig. 2a).

Airfall pumice deposit (site 2)

Site 2 is an airfall pumice deposit, derived from the 2360 BP eruption of the Mount Meager Volcano, and overlies a coarse regolith as shown at road level in Fig. 2b. The deposit comprises a loose framework of angular dacitic pumice fragments up to 20 cm in diameter and small amount of fine matrix. The deposit has little internal structure, except in the top few decimeters where there is some crude layering derived from reworking. The measured thickness of the deposit is 3.6 m, although this thickness varies throughout the deposit due to locally controlled, post-depositional erosion and slumping.

The GPR data were collected along a 50-m traverse over the airfall pumice deposit above a logging road (Fig. 2b; Table 1). The data are displayed in Fig. 4 with no vertical exaggeration and minor gain. Several traces show little or no received signal, which is due to poor surface coupling of the antennae where the survey crossed a steep slope covered in clear-cut forest debris. Most traces, however, show strong air and ground wave arrivals and a strong event around 100 ns which we interpret to be the base of the airfall pumice deposit. Above this reflection the data show few coherent reflections; there is some indication of stratification in the central part of the deposit over the first 20 m. These radar characteristics are consistent with the relatively structureless and well-sorted character of the deposit. The weakly reflected energy from the interior of the deposit may be due to the larger pumice blocks with dimensions near the resolution limit of the instrument (decimeter scale).

The measured depth of the pumice deposit (3.6 m), shown as a circle in Fig. 4b, was used to determine an average velocity of 0.07 m/ns for EM wave propagation through the deposit. Also shown in Fig. 4b is the interpreted, irregular base of the pumice fall deposit. The loss of radar signal beneath the pumice layer probably results from the high electrical conductivity of the underlying colluvium.

Pyroclastic flow deposit (site 3)

Downstream from Mount Meager, near the confluence of the Lillooet River and Pebble Creek, is a 20-m-high stream-dissected bluff (Fig. 2c) containing unconsolidated pyroclastic deposits (Stasiuk and Russell 1990). A 192-m-long GPR traverse was run along a flat bench immediately above this bluff. At the top of the exposure are thinly stratified stream deposits approximately 2 m thick, underlain by a crudely layered mudflow deposit approximately 5–7 m thick which thins southward along the exposure. The remainder of the section comprises two distinct pyroclastic block and ash flow units which have a combined thickness of 9 m (Stasiuk and Russell 1990). The deposits of the two pyroclastic flow units are chaotic, structureless, poorly sorted mixtures of large (0.5–1 m), rounded blocks of pumice, pumice lapilli, and abundant ash-lapilli sized matrix. The upper pyroclastic flow unit contains abundant charred logs, stumps, and branches (Fig. 2d). The lower pyroclastic flow deposit rests on a thin (<40 cm) layer of ash which is underlain by a clay-rich soil horizon.

The GPR survey comprises seven segments (Fig. 5a) oriented roughly parallel to the face of the bluff. The exposure in Fig. 2c is located approximately at the center of the GPR profile. The corresponding GPR data are shown in Fig. 5b, c, and d plotted at the same gain but with different vertical exaggerations. Figure 5b shows three distinct and labeled parts to the profile including: (a) an upper, southward-thinning, stratified deposit that corresponds well with the observed stratified deposits in the bluff; (b) a central, structureless zone

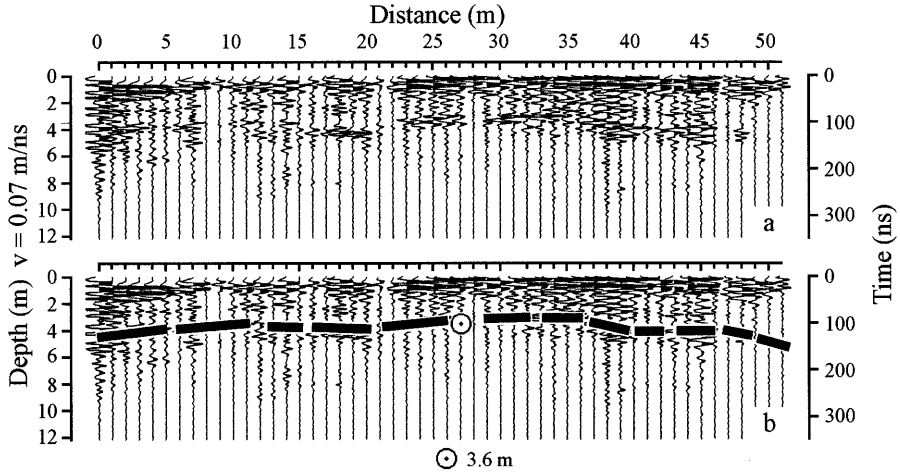

Fig. 4a, b Radar profiles for pumice fall deposit (site 2) are displayed with no vertical exaggeration and an AGC gain of 0.002. **b** shows the interpreted basal contact for the deposit (*heavy dashed line*) against a single field measurement of deposit thickness (*circle*)

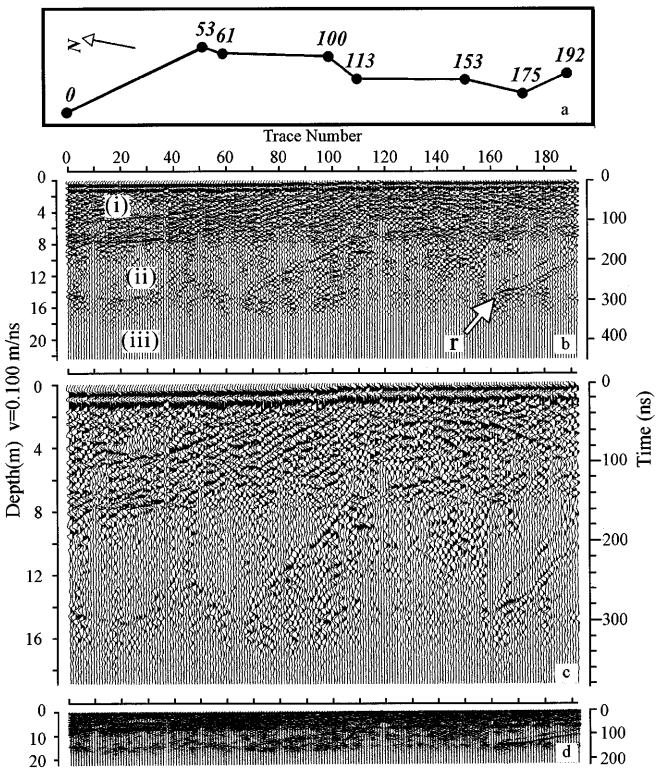

Fig. 5a–d Radar profiles for the pyroclastic flow section (site 3). Traverse comprises seven segments which crudely parallel the cliff face (Fig. 2c): orientations of individual lines (total of 192 m) are shown schematically in **a**. GPR results are shown with vertical exaggeration of **b** 3×, **c** 6×, and **d** 1× and AGC gains of 0.008, 0.008, and 0.01, respectively. See text for discussion of specific features

with a reasonably well-defined base at a depth of approximately 16 m; and (c) a lower "dead" zone.

The central zone shows diffuse areas of chaotic but strong reflections, particularly visible at a distance of approximately 70–110 and 140–160 m. This pattern is at least partially a result of overlapping point diffractor hyperbolae; the rounded apex of a relatively clear hyperbola is visible in Fig. 5c at a time of approximately 200 ns and a distance of approximately 90 m. We interpret the central structureless zone as the pyroclastic flow deposits and the hyperbolic events as diffractions from large pumice blocks or charred tree trunks. Farther to the south, starting at a distance of approximately 165 m, is a shallowly inclined north-dipping reflector (r, Fig. 5b) which correlates with the interface between the two pyroclastic flow deposits. Although this ramp-like structure is clearly defined in the GPR profile, it is a more subtle feature in the outcrop and probably reflects slight variations in grain-size distributions between the top of the lower unit and the base of the overlying pyroclastic flow.

The top of the dead zone, below the pyroclastic flow deposits, corresponds to the contact between the lowest pyroclastic unit and the underlying paleosol. Enhanced conductivity of the underlying sediments is the most likely reason for the severe attenuation of the radar signal at this depth.

Pumice talus cone (site 4)

On the north side of Mount Meager (Fig. 1), the Lillooet River cuts through a 100-m sequence of unconsolidated pyroclastic deposits (Fig. 2f) overlying an older unconsolidated, poorly sorted, matrix-rich rock avalanche deposit. The pyroclastic deposits comprise complex, meter-scale layers of mantling, well-sorted airfall pumice beds and poorly sorted, channel-filling, structureless beds of moderately rounded pumice clasts and ash. The pyroclastic section represents a proximal accumulation of tephra during the 2360 BP eruption of Mount Meager (Nasmith et al. 1967; Clague et al. 1995) and has been interpreted as a talus cone of material periodically slumped from oversteepened upper slopes during fallout from a pyroclastic column. The channels are typically tens of meters wide and cut several meters into the underlying beds (Fig. 2f). In the bluff exposure the contact between the tephra and the avalanche deposit occurs in the lower third of the cliff face and is sharp and nearly horizontal (Fig. 2e and f).

The GPR traverse follows a logging road on top of the bluffs (Fig. 2e; Table 1) and is situated 30–50 m back from the cliff face. At this site field conditions prevented accurate measurement of the deposit thicknesses immediately below the GPR survey stations and, thus, an intermediate radar velocity of 0.09 m/ns was used (Table 2).

Two separate traverses were performed: a longer traverse which used relatively coarse spacing and long time windows, and a shorter traverse using finer spacing and short time windows (Table 1). The coarse spacing inhibits resolution of complex, finer-scale stratification, but the traverse length and long time window favor detection of deep, sharp, laterally extensive contacts. The shorter, more finely spaced GPR traverse was conducted to investigate shallow, fine structure.

Table 2

Site	Deposit	Reflector used	V_{field} (m/ns)	$K'_{field}=(c/V)^2$
1	Basalt lava flow	Base of basalt lava flow	0.09	11.1
2	Pumice fall deposit	Base of pumice overlying alluvium	0.07	18.4
3	Pyroclastic flow	Base of pyroclastic flow overyling paleosol	0.1	9
4	Pumice talus cone	None available	N/A	N/A

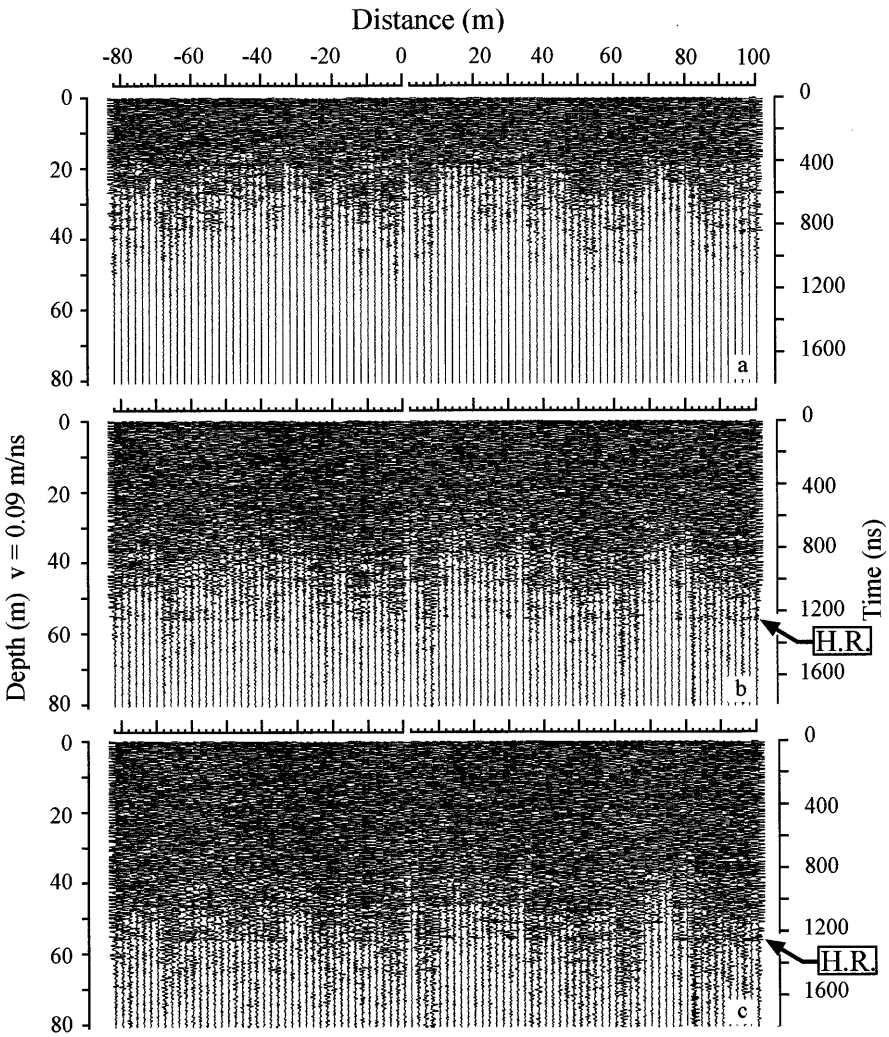

Fig. 6a–c Radar profiles for data collected over the pumice talus deposit (site 4a). Traverse results are shown with no vertical exaggeration and AGC gains of **a** 0.01, **b** 0.05, and **c** 0.1. Fine-scale shallow structures are lost due to saturation of shallow signals and coarse station spacing (2 m), whereas survey results delineate a prominent near-horizontal reflector (H.R.) at approximately 55 m (1225 ns)

Figure 6 shows the deep GPR profile at three different levels of gain and with no vertical exaggeration. With increasing gain, the upper parts of the profile become saturated as significant reflections at increasing depth become observable (Fig. 6a, b, and c). There are no major reflections evident in the uppermost portion (<50 m) of the profile, even with substantial gain (e.g., Fig. 6b). In Fig. 6b and c there is a nearly horizontal feature at a depth of approximately 55 m (labeled H.R.), which is also paralleled by several weaker reflections. This is an extreme depth for GPR of 400 MHz frequency in rock and it is at such depths where the magnitude of coherent noise generated by the instrument (see Appendix) is expected to be large relative to most real reflected signals. The reality of observed deep features in GPR profiles must therefore be cautiously considered. In this case (Fig. 6) the feature in the geophysical profile compares well in terms of orientation, depth, continuity, and prominence with a real feature in the exposure: the basal contact of the tephra overlying the rock avalanche. Furthermore, a detailed comparison of the data with coherent noise generated by the instrument (see Fig. A1) shows that the feature in the profile is not well explained as an artifact. On this basis we argue that the feature is real and represents the basal contact, although confirmation would require continuing the survey to locations where the contact shallows. The results from this site indicate that the technique has good potential for delineating deposits of considerable thickness. The results also underline the necessity of calibrating the instrument where the deposits are clearly exposed.

The results of the shorter finer-spaced GPR traverse elucidate some of the shallower features of this thick accumulation of tephra. The data are presented in Fig. 7 as identical GPR sections, except that Fig. 7b is interpreted. The profiles show bedding structures of the same form and size as observed in the bluffs (Fig. 2f). As outlined in Fig. 7b, the GPR data define at least one prominent channel approximately 35 m wide and 5 m deep infilled with a lens of predominantly structureless material and overlain by stratified beds.

Laboratory measurements of *K'*

The GPR field studies described above cover a wide range of deposit types which are diverse in character,

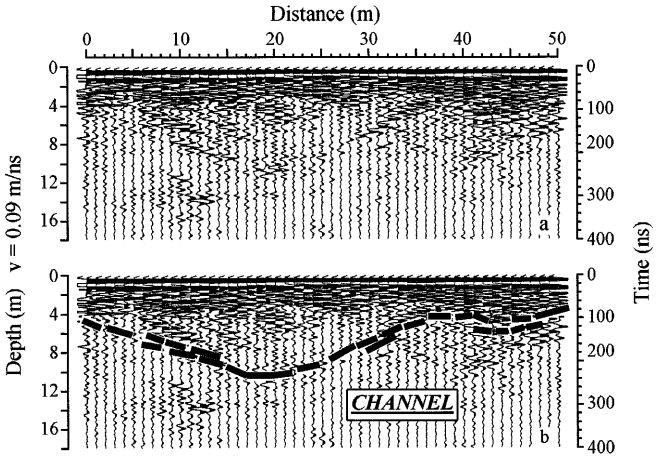

Fig. 7a, b Radar profiles for traverse over the pumice talus deposit showing fine-scale, shallow structures (site 4b; Table 1). **a** Data and **b** interpretation of channel structure are shown with no vertical exaggeration

structure, and composition. Velocities of radar signals in these deposits have been estimated from the field data and are shown to vary significantly (Table 2). Velocities can also be estimated from laboratory measurements of dielectric properties. Under conditions of low loss, where GPR performs well, velocity (V) is related to the dielectric constant (K') by:

$$V = \frac{c}{\sqrt{K'}} \quad (1)$$

where c is the propagation velocity of electromagnetic waves in free space (e.g., Davis and Annan 1989).

One approach, therefore, is to assign velocities to deposits based on measured dielectric properties of the rocks. Because of the importance of velocity estimates for converting GPR data into accurate geological subsurface maps, we measured values of K' for four volcanic rock types (Table 3) pertinent to the GPR field studies. These data complement the growing database of dielectric properties for geological materials such as sandstones (e.g., Knight and Nur 1987), basalts (e.g., Hansen et al. 1973; Drury 1978; Frisillo et al. 1975; Singh and Singh 1991) and a variety of other volcanic, plutonic, and metamorphic rocks (e.g., Singh and Singh 1991; Ulaby et al. 1990). Lastly, these laboratory measurements afford an opportunity to compare both lab and field estimates of dielectric properties and implied velocities.

Laboratory results

The laboratory measurements were made in the Rock Physics Laboratory at The University of British Columbia using modified methods of Knight and Nur (1987). Samples were prepared as thin disks approximately 5 cm in diameter and 0.5 cm in thickness. Top and bottom surfaces of sample disks were sputtered with a thin, uniform, 50-nm-thick layer of gold to form the electrodes. Dielectric constant experiments on each sample disk comprised sampling at 25 frequencies over the frequency range 10 Hz and 10 MHz. Porosity of individual samples was also measured with a helium porosimeter (Knight and Nur 1987; Knight and Endres 1990) and is reported in Table 3.

Values of K' were measured for basalt lava from site 1, a block of dacite pumice from site 3 (Stasiuk and Russell 1990), a dense obsidian breccia from Mount Meager, and dacite lava from Mount St. Helens. Multiple cores were taken from each rock and a sample disk was prepared from each core, making a total of ten disks (Table 3). Individual sample disks were analyzed at least twice by loading the samples so that each gold-sputtered surface faced up and then down in the sample holder. Several samples were analyzed five or more times in a fixed orientation, thereby establishing an empirical baseline of instrument precision; the variance due to instrument noise is negligible. Furthermore, variances in measurement resulting from loading procedure (e.g., flipping sample in holder and repeating measurement) are also insignificant.

Table 3 Least-squares regressions of K' measured over frequency (λ) interval 10 Hz – 10 MHz for cores of select volcanic rocks. Data are reported as $K' = A \log(\lambda) + B$ and as values of K'_{100} extrapolated to 100 Mhz. The mean calculated velocity (V_{100}) and measured porosity (P) of samples are reported with the associated 1 standard deviation in the measurement

Rock type/sample no.	Core (N)	A	B	R^2	K'_{100}	V_{100} (m/ns) ± 1 s	P (%) ± 1 s
Basalt (MMGPR-19)	1a (2)	−0.2905	9.612	0.999	9.031		
Cheakamus Valley	1b (2)	−0.3328	9.858	0.999	9.192	0.0998 ± 0.0014	9.13 ± 0.80
	2 (2)	−0.1886	9.124	0.994	8.746		
Dacite Pumice (MMGPR-8)	1a (2)	−0.05366	4.215	0.989	4.108		
Mt. Meager	1b (2)	−0.04918	4.284	0.991	4.185	0.1495 ± 0.0038	39.47 ± 2.71
	2 (2)	−0.05824	3.922	0.984	3.805		
Dacite breccia (MMGPR-16)	a (2)	−0.1259	7.992	0.986	7.740	0.1079 ± 0.0001	11.09 ± 0.42
Mt. Meager	b (2)	−0.1256	7.975	0.987	7.724		
Dacite lava (MSH-87-3b)	a (2)	−0.04572	5.465	0.979	5.373	0.1294 ± 0.00	27.71 ± 0.49
Mount St. Helens	b (2)	−0.04333	5.462	0.978	5.375		

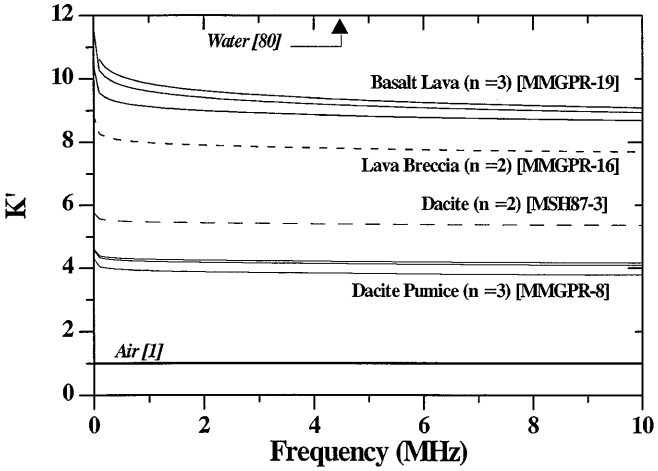

Fig. 8 Laboratory-measured dielectric constants (K') for volcanic materials (see text) measured over the frequency range 10 Hz to 10 MHz. *n* number of sample cores measured

Figure 8 is a graphic summary of the experimental measurements. The highest values of K' derive from the three sample disks prepared from cores of the Cheakamus basalt which has a mean porosity (vesicularity) of 9.1%. The mean values for each sample disk have been independently fitted by least-squares analysis to a model line (Table 3). The regressions are used to extrapolate the experimental measurements of K' to an appropriate value expected at higher operational frequencies (e.g., 100 MHz, K'_{100}; Table 3). The observed range of values of K'_{100} for the basalt is 8.7–9.2, which lies within the range of values of K' for basalt (7–15) measured by Hansen et al. (1973) at 50 MHz.

Measurement uncertainty (e.g., instrument noise, loading procedure, etc.) is no larger than the thickness of the solid lines representing the fits to the data. The three cores have significantly different values of K', although the between-disk variation is small compared with the range shown for all four rock types. The between-disk variation must represent sample heterogeneity arising from small-scale structural and mineralogical variations within the basalt.

The next highest values of K' derive from measurements made on two cores from a welded dacite obsidian breccia, both with 11% porosity. There is virtually no between-sample variation of K'_{100} (7.72–7.74) suggesting that, in terms of dielectric properties, the material is homogeneous, despite the fact that the sample is a hyalocrystalline breccia. The data acquired from two cores of dacite collected from the Mount St. Helens dome lavas show similar behavior. The lava comprises a subequal mixture of glass, crystals, and vesicles; the measured porosity is 27–28%. The values of K' measured on these two cores are indistinguishable ($K'_{100}=5.37$) and plot as a single line (Fig. 8). The lowest values of K' derive from three sample disks of pumice collected from the pyroclastic flow at site 3. These samples have a mean porosity of 39.5% and also show significant between-sample variation ($K'_{100}=3.8$–4.2) indicating that in terms of dielectric properties the pumice is heterogeneous.

Implications of measured K'

Field vs laboratory dielectric properties

Our laboratory measurements show that volcanic rocks can have significantly different dielectric properties (Fig. 8), and these variations imply significant differences in electromagnetic velocities (0.1–0.15 m/ns). Velocity is a critical parameter in terms of creating accurate subsurface geological maps from radar data, and Fig. 9 compares laboratory-estimated and field-constrained velocities. The inset to Fig. 9 shows the relationship (Eq. (1)) between K' and velocity. Plotted on the curve, and showing little overlap, are the laboratory-measured values of K'_{100} (open circles) for the ten sample disks and the three field-estimated velocities for sites 1–3 (solid circles; Table 2).

The discordance between laboratory-measured and field-estimated dielectric properties of these specific volcanic deposits is shown explicitly in the main part of Fig. 9, where the two estimates of velocity are plotted. In each of the three cases where a field estimate of electromagnetic velocity can be determined, the corresponding laboratory measurement always returns a higher velocity. The best agreement is for site 1, the survey over the Cheakamus basalt lava flow, because the deposit is massive and homogeneous, except for large-scale fractures and joints. The greatest discrepancy is between the field estimated velocity on the pumice fall deposit (site 2) and the range of velocities measured on pumice samples (0.07 vs 0.13–0.15 m/ns). The laboratory measurements are an inadequate characteri-

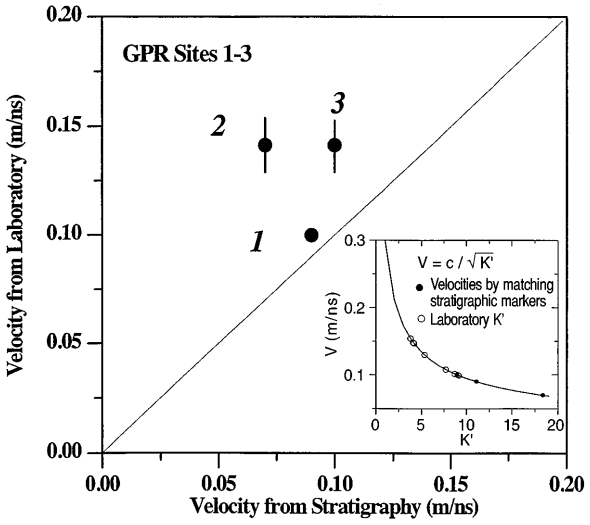

Fig. 9 Radar velocities inferred from field calibration of GPR profiles on stratigraphic horizons compared with velocities calculated from laboratory measured values of K'_{100} (see *inset*)

zation of the pumice fall deposit, even though the deposit is well-sorted and comprises more or less uniform-sized pumice pieces. Less surprising is the discordance in velocity estimates for the pyroclastic flow (site 3). The laboratory measurements were made on pumice blocks which, although comprising a substantial portion of the deposit, could not be construed as representative of its bulk character.

To a large extent, the discordance between laboratory and field estimates of velocity derives from differences between the nature of the deposit and what is actually used as a sample in the laboratory measurement. Unfortunately, we do not yet have the ability to predict effective electromagnetic velocities in geological deposits based on simple laboratory-measured dielectric properties. Consequently, the velocities needed to convert GPR data into meaningful geological cross sections must derive from calibration of GPR surveys against well-exposed deposits or from Common Midpoint Surveys (e.g., Davis and Annan 1989; Pilon et al. 1991). This situation will presumably continue until there is a greater understanding of how grain size, sorting, and clast composition control the bulk dielectric properties of geological deposits (e.g., Knight and Endres 1990; Knoll and Knight 1994).

Variations in dielectric properties of volcanic rocks

Based on the laboratory data presented in Fig. 8 and Table 3, several points can be made concerning the dielectric properties of volcanic rocks. These points have direct relevance for future applications of GPR to field-based volcanological studies, because of the relationship between dielectric properties and EM velocity.

Firstly, as shown in Fig. 10, measured values of K'_{100} and sample porosity are strongly linked; increasing porosity dictates a lower value of K'_{100}. Under these experimental conditions, porosity seems to be a first-order effect as compared with the effects of other rock properties such as chemical composition, modal mineralogy, proportion of glass, or grain size. This strong control of porosity on dielectric property suggests a number of important field applications for GPR. Using GPR it should be possible to map variations in primary porosity (vesicularity) in volcanic deposits and, for example, to delineate zones of brecciation or to distinguish between welded and unwelded portions of ignimbrite sheets.

A second point concerning sample porosity relates to experimental methodology. The data in Fig. 8 show two types of behavior. Two samples show virtually no variation in dielectric property between cores, whereas there is significant between-core variance for the basalt and pumice (Table 3). This behavior does not correlate with the absolute porosity of the samples, but there is a direct correlation between the relative variance in sample porosity and the between-core variation in dielectric properties (inset, Fig. 10). Cores of samples that showed little variation in porosity (e.g., MMGPR-16) had virtually identical values of K'_{100}, and samples which yielded cores of widely varying porosity (e.g., MMGPR-19) showed significant variation in K'_{100}.

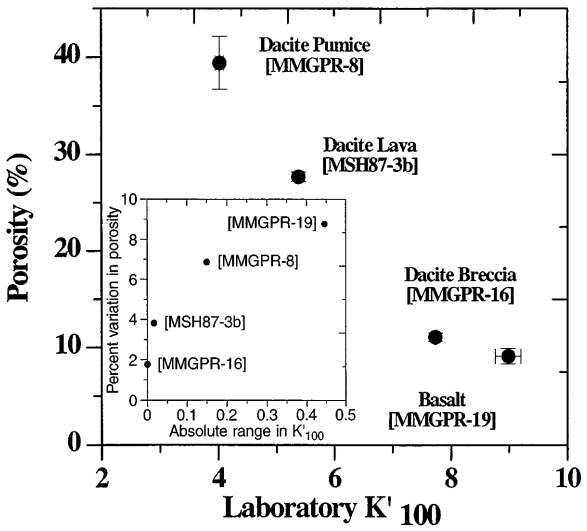

Fig. 10 Laboratory-measured mean values of K'_{100} and porosity plotted for four volcanic rock samples (Table 3); variations in measurements are represented as 1-σ error bars. *Inset* shows the correlation between sample-scale variations in K'_{100} and vesicularity or porosity (see text)

Both the dacite breccia and the dacite lava samples have homogeneous physical properties. For the breccia this results from the fact that it is 70% volcanic glass and is very densely welded, a process which reduces original pore space and obliterates clast boundaries. The Mount St. Helens dacite lava has a significantly lower but constant value of K'_{100} (5.37) reflecting the higher vesicularity of the sample. The homogeneous dielectric properties of these samples suggest a uniform distribution and abundance of crystals, vesicles, and glass in the lava at the scale of the sample disks. This is corroborated by the small range in measured porosity (2%).

In contrast, the values of K'_{100} for the pumice are low and show high variability. Both features can be attributed to a single cause: high and variable porosity at the scale of sample preparation. These three cores have the highest porosity of all four rock types (39% Ave.) but also show a large range of values (7%). Notably, the basalt has an even greater (9%) relative variation in porosity (Fig. 9; Table 3) suggesting that the between-sample variation seen in the basalt cores also reflects heterogeneity in vesicle distribution on the scale of the sample disks.

Discussion

Several broad conclusions derive from this study. Firstly, results from the four traverses show that, even with-

out extensive processing, GPR can be extremely effective in defining the bases of volcanic deposits down to depths of 55 m. As such, GPR has tremendous potential for quantifying distributions, thicknesses, and volumes of volcanic deposits. For example, isopach maps of airfall tephras could be constructed far more easily, rapidly, and completely with GPR than by digging. Secondly, several of our traverses demonstrate that GPR can elucidate finer-scale internal structures of volcanic deposits, suggesting a means for studying facies variations within individual units or for mapping deposits with complex geometries in the subsurface.

Furthermore, if data from these four traverses are taken collectively, it appears that volcanic deposits with different characteristics (e.g., grain-size variations, internal structures, etc.) interact with the radar beam in distinct ways, with the result that individual deposit types may be expected to have "characteristic" geophysical signals. This suggests that, with sufficient experience, some types of volcanic deposit might be recognized on the basis of their geophysical character in cases where there is no surface exposure.

We note that other frequencies of radar could be used (e.g., Davis and Annan 1989; Jol and Smith 1991) to obtain deeper penetration (lower frequencies) or better resolution (higher frequencies) depending on the objectives of the study. In addition, processing could help improve the interpretability of images of complex geometries.

Our laboratory measurements on volcanic rocks show a clear and poorly understood discordance between the laboratory-measured and field-estimated values of *K'*. Consequently, it is clear that calibrating the signal at well-exposed sections is important. This also permits the selection of optimal gain levels, time window, and station spacing, and permits the rough association of signal character with a deposit type.

Appendix: Ancillary technical and operational details

The radar signal emitted from the transmitting antenna comprises pulses of electromagnetic radiation of a restricted frequency spectrum. The center of the spectrum and dominant proportion of the emitted power is at the stated frequency for the antenna. The upper and lower limits are at 150 and 50% of the stated frequency, respectively. Transmitted pulses propagate as air waves above the substrate, as surface waves along the air–substrate interface, and as body waves within the substrate. The body wave energy is gradually attenuated and scattered by reflections from material discontinuities. Reflected energy returns to the surface where it generates voltage fluctuations in the receiving antenna, recorded as a trace. The period over which reflections from a single emitted pulse are recorded is the time window. Because the path is shortest and speed typically greatest for the air and surface waves, these are the first received and start each trace. The energy from each emitted pulse in the series has the same travel path, so that the resulting traces are identical except for superimposed noise. Averaging traces at a station (stacking) produces destructive interference of random noise while preserving the consistent part of the signal; the number of averaged traces is the number of stacks.

Coherent (non-random) noise, which is not removed by stacking, can also occur. The GPR equipment itself is one source of weak, coherent noise; Figure A1 shows an artificial profile generated by sampling the ambient noise field (without transmitting). The data are displayed using the same parameters as used in Fig. 6 (Site 4a). Where displayed with significant gain, a series of flat "reflections" appears. These features are distinctive and non-physical in that they always occur at the same times (depths), and they do not attenuate with depth. This non-random noise is present in all the profiles, but for the most part has insignificant amplitude relative to the received signals and hence is not visible. The 55-m reflection seen in the deep profiles of site 4 (e.g., Fig. 6b) is interpreted to be real, because it does not occur at the same depth (time) as any of the artifacts

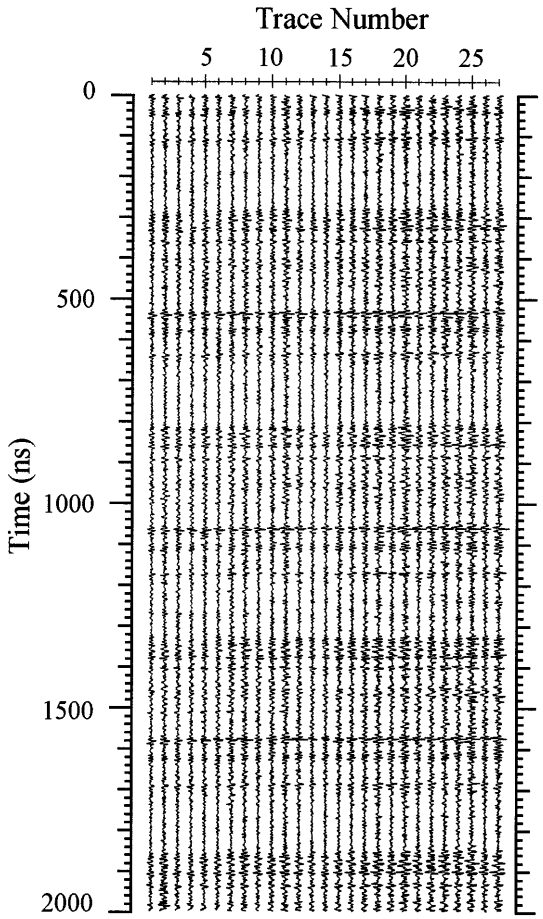

Fig. A1 Radar section-styled display of instrument noise for the pulseEKKO IV ground-penetrating radar device. Radar traces result from repetitive collection of signal over a time window of 2048 ns with the transmitter off. Data are shown with a nominal AGC gain of 0.02

seen in Fig. A1. Furthermore, its amplitude is large and not repeated at greater depths. In Fig. 6c (higher gain) several weak reflectors are just discernible above and below 55 m; these occur at times close to artifacts shown in Fig. A1 and may represent noise.

Acknowledgements Field logistical costs (1992) were covered by EMR contract 23254-3–1032/01-XSB in association with Dr. C. J. Hickson as part of the Mount Meager Project. Ancillary research costs were borne by NSERC operating grant A0820 (J. K. R.). We also acknowledge Dr. R. J. Knight for access to both GPR and Rock Physics Laboratory instrumentation. The authors benefited greatly from practical instruction and beneficial discussions with J. Rea, P. Tercier, and especially M. Knoll. Laboratory measurements were made by A. Dubin with support from the B. C. Challenge Work-Studies program. Reviews by M. Rossi and D. Pieri helped improve our presentation and the clarity of our arguments. Results and interpretations presented herein are solely the views of the authors.

References

Annan AP, Davis JL (1977) Radar range analysis for geological materials. Geol Surv Can Pap 77–1B:117–124

Ardon OFP (1985) Comparison among seismic refraction, electrical resistivity and ground probing radar methods for shallow underground structure investigation. Individual Studies by Participants at the International Institute of Seismology and Earthquake Engineering 21:83–98

Camerlynck C, Dabas M, Panissod C (1994) Comparison between GPR and four electromagnetic methods for stone features characterization: an example. Archeol Prospect 1:5–17

Clague JJ, Evans SG, Rampton VN, Woodsworth GJ (1995) Improved age estimates for the White River and Bridge River tephras, western Canada. Can J Earth Sci 32:1172–1179

Clarke KC, Cross GM (1989) Radar imaging of glaciovolcanic stratigraphy, Mount Wrangell caldera, Alaska: interpretation , model and results. J Geophys Res 94:7237–7249

Davis JL, Annan AP (1989) Ground-penetration radar for high-resolution mapping of soil and rock stratigraphy. Geophys Prospect 37:531–551

Drury MJ (1978) Frequency spectrum of the electrical properties of seawater-saturated ocean crust and oceanic island basalts. Can J Earth Sci 15:1489–1495

Fowler JC (1981) Subsurface reflection profiling using ground-probing radar. Mining Engineer 33 (8):1266–1270

Frisillo AL, Olhoeft GR, Strangway DW (1975) Effects of vertical stress, temperature and density of the dielectric properties of lunar samples 72441, 12, 15301, 38 and a terrestrial basalt. Earth Planet Sci Lett 24:345–356

Gilbert JS, Stasiuk MV, Lane SJ, Adam CR, Murphy MD, Sparks RSJ, Naranjo JA (1996) Non-explosive, constructional evolution of the ice-filled caldera at Volcan Sollipulli, Chile. Bull Volcanol 58:67–83.

Goodman D (1994) Ground-penetrating radar simulation in engineering and archeology. Geophysics 59:224–232

Green NL, Armstrong RL, Harakal JE, Souther JG, Read PB (1988) Eruptive history and K–Ar geochronology of the late Cenozoic Garibaldi volcanic belt, southwestern British Columbia. Geol Soc Am Bull 100:563–579

Hansen W, Sill WR, Ward SH (1973) The dielectric properties of selected basalts. Geophysics 38–1:135–139

Hatton L, Worthington MH, Makin J (1986) Seismic data processing, theory and practise. Blackwell, Oxford

Holloway AL Soonawala NM, Collett LS (1986) Three-dimensional fracture mapping in granite excavations using ground-penetrating radar. Can Inst Mining Bull 79:54–59

Jezek KC, Thompson LG (1982) Interpretation of mono-pulse ice radar soundings on two Peruvian glaciers. IEEE Trans Geosci Remote Sensing GE-20 (3):243–249

Jol HM, Smith DG (1991) Ground penetrating radar of northern lacustrine deltas. Can J Earth Sci 28:1939–1947

Jol HM, Smith DG (1992) Geometry and structure of deltas in large lakes: a ground-penetrating radar overview. Geol Surv Finland, Special Paper 16:159–168

Knight RJ, Endres AL (1990) A new concept in modeling the dielectric response of sandstones: defining a wetted rock and bulk water system. Geophysics 55:586–594

Knight RJ, Nur A (1987) The dielectric constant of sandstones, 60 kHz to 4 Mhz. Geophysics 52:644–654

Knoll MD, Knight RJ (1994) Relationships between dielectric and hydrogeologic properties of sand-clay mixtures. Fifth Int Conf Ground Penetrating Radar, Kitchener, Canada

Knoll MD, Haeni FP, Knight RJ (1991) Characterization of a sand and gravel aquifer using ground-penetrating radar, Cape Cod, Massachusetts. USGS Water Res Invest Rep 91–4034:29–35

Liner CL, Liner JL (1995) Ground-penetrating radar: a near-face experience from Washington County, Arkansas. Leading Edge 18:17–21

McCoy FW, Papmarinopoulos S, Doumas C, Palyvou C (1992) Probing the Minoan eruption on Thera with ground-probing radar: buried extent of Akrotiri, tephra stratigraphy and late-bronze-age volcanic hazards. Geol Soc Am 1992 Annual Meeting Program with abstracts 24:26

Nasmith H, Mathews WH, Rouse GE (1967) Bridge River ash and some other Recent ash beds in British Columbia. Can J Earth Sci 4:163–170

Nicholls J, Stout MZ, Fiesinger DW (1982) Petrologic variations in Quaternary volcanic rocks, British Columbia, and the nature of the underlying upper mantle. Contrib Mineral Petrol 79:201–218

Pilon JA, Grieve RAF, Sharpton VL (1991) The subsurface character of Meteor Crater, Arizona, as determined by ground-probing radar. J Geophys Res 96:15563–15576

Pratt BR, Miall AD (1993) Anatomy of a bioclastic grainstone megashoal (Middle Silurian, southern Ontario) revealed by ground-penetrating radar. Geology 21:223–226

Rea J, Knight R, Ricketts BD (1994) Ground-penetration radar survey of the Brookswood aquifer, Fraser Valley, British Columbia. Geol Surv Can Pap 1994-A:211–216

Read PB (1977) Geology of Meager Creek geothermal area, British Columbia. Geol Surv Can Open File 603

Singh J, Singh PK (1991) Studies of the dielectric constant of Indian rocks and minerals and some other materials. Pageoph 135:601–610

Smith DG, Jol HM (1992) Ground-penetrating radar investigation of a Lake Bonneville delta, Provo level, Brigham City, Utah. Geology 20:1083–1086

Stasiuk MV, Russell JK (1990) The Bridge River assemblage in the Meager Mountain volcanic complex, southwestern British Columbia. Geol Surv Can Pap 90–1E:153–157

Stasiuk MV, Russell JK (1993) Preliminary studies of Recent volcanic deposits in southwestern British Columbia using ground penetrating radar. Geol Surv Can Pap 94-A:151–157

Ulaby FT, Bengal TH, Dobson MC, East JR, Garvin JB, Evans DL (1990) Microwave properties of dry rocks. IEEE Trans Geosci Remote Sensing 28:325–336

Vaughan CJ (1986) Ground-penetrating radar survey used in archeological investigations. Geophysics 51:595–604